

# Glioma Expansion in Collagen I Matrices: Analyzing Collagen Concentration-Dependent Growth and Motility Patterns

L. J. Kaufman,<sup>†§</sup> C. P. Brangwynne,<sup>\*</sup> K. E. Kasza,<sup>\*</sup> E. Filippidi,<sup>\*</sup> V. D. Gordon,<sup>†</sup> T. S. Deisboeck,<sup>‡¶</sup> and D. A. Weitz<sup>\*†</sup>

<sup>\*</sup>Division of Engineering and Applied Sciences, and <sup>†</sup>Department of Physics, Harvard University, Cambridge, Massachusetts;

<sup>‡</sup>Molecular Neuro-Oncology Laboratory, Massachusetts General Hospital, Charlestown, Massachusetts; <sup>§</sup>Center for Imaging and Mesoscale Structures, Harvard University, Cambridge, Massachusetts; and <sup>¶</sup>Complex Biosystems Modeling Laboratory, Harvard-MIT (HST)

Athinoula A. Martinos Center for Biomedical Imaging, Massachusetts General Hospital, Charlestown, Massachusetts

**ABSTRACT** We study the growth and invasion of glioblastoma multiforme (GBM) in three-dimensional collagen I matrices of varying collagen concentration. Phase-contrast microscopy studies of the entire GBM system show that invasiveness at early times is limited by available collagen fibers. At early times, high collagen concentration correlates with more effective invasion. Conversely, high collagen concentration correlates with inhibition in the growth of the central portion of GBM, the multicellular tumor spheroid. Analysis of confocal reflectance images of the collagen matrices quantifies how the collagen matrices differ as a function of concentration. Studying invasion on the length scale of individual invading cells with a combination of confocal and coherent anti-Stokes Raman scattering microscopy reveals that the invasive GBM cells rely heavily on cell-matrix interactions during invasion and remodeling.

## INTRODUCTION

The brain tumor glioblastoma multiforme (GBM) accounts for 23% of all primary brain tumors (1). It is a highly invasive tumor, which renders complete surgical excision of the cancerous tissue impossible, thus explaining the neoplasm's poor prognosis, with a 5-year relative survival rate of ~2% in 45- to 64-year old patients (1). A better understanding of the factors that allow for such swift GBM tumor invasion, including details of cell-extracellular matrix (ECM) interactions, are critically important in the goal of developing novel, more effective strategies to treat this cancer.

Using an *in vitro* GBM model, this study examines the growth of a multicellular brain tumor spheroid (MTS) and the invasion of its migratory brain tumor cells into three-dimensional (3D) collagen I matrices. These matrices differ in collagen concentration and thus in average stiffness and mesh size. We study the growth and invasion of the GBM system in these matrices on two length scales, that of the entire system and that of individual invasive cells interacting with collagen fibers. Three-dimensional collagen matrices have been used previously in studies of the migration of fibroblasts (2–7), leukocytes (8), lymphocytes (9), and metastatic tumor cells (10–14). Such studies have found that cell migration in 3D matrices differs substantially from that on two-dimensional (2D) substrata. For example, it has been shown that fibroblasts develop different focal contacts in 3D

collagen matrices than on 2D substrata (3,15). Although most of the aforementioned studies of cells in 3D matrices have focused on the importance of various integrins in adhesion and detachment events as well as the role of matrix metalloproteinases (MMPs) in migration, this study focuses on the mechanical aspects of migration. We believe it is crucially important to consider both how cells affect their surroundings and how these surroundings affect the cells during migration. Though there have been a number of studies indicating that cells have different spreading behavior and migratory responses when plated on surfaces of different ECM protein concentration (16–21), studies of this type are not commonly performed in 3D matrices even though such matrices are a closer approximation to the *in vivo* surroundings of most cells, since they do not have a pronounced asymmetry with respect to the dorsal and ventral sides of the cell.

In a recent study, Gordon et al. (22) showed that two competing mechanical forces are important during GBM growth and invasion in a 3D matrix: rapid volumetric expansion of the MTS induces mechanical stress in the surrounding gel matrix, whereas invading cell tips exert traction on the matrix. In that study, GBM MTSs, or spheroids, were placed in a Matrigel matrix, composed chiefly of collagen IV, laminin, entactin, and heparan sulfate proteoglycans. Matrigel consists of interconnected protein sheets and appears rather homogeneous in phase-contrast microscopy. The finding of Gordon et al. (22) that cells exert traction during cell process extension agrees with the findings of others for 2D cell migration. Indeed, a large body of work exists that aims to quantify cell-traction forces in two dimensions (16,18,23–31). The work of Roy et al. (23), in particular, revealed that corneal fibroblasts plated on a collagen matrix exert traction forces during both cell process extension and partial cell process retraction and that the matrix

---

Submitted February 25, 2005, and accepted for publication April 21, 2005.

Address reprint requests to Laura Kaufman, Dept. of Chemistry, Columbia University, New York, NY 10027. E-mail: kaufman@chem.columbia.edu.

Vernita Gordon's present address is School of Physics, University of Edinburgh, Edinburgh, EH8 3JZ, Scotland.

Laura Kaufman's permanent address is Dept. of Chemistry, Columbia University, New York, NY 10027.

© 2005 by the Biophysical Society

0006-3495/05/07/635/16 \$2.00

doi: 10.1529/biophysj.105.061994

is released only during total pseudopod retraction. In recent years, studies have also been done that attempt to quantify the forces exerted by cells in 3D matrices (32). The traction exerted by the invasive GBM cells in the 3D Matrigel, which appears similar to that applied by cells on a 2D substrata, strongly suggests that local matrix remodeling occurs during GBM cell migration.

Matrix remodeling by cells has been studied globally by monitoring the shrinkage of a collagen surface or matrix (2,33,34). Matrix remodeling has also been studied locally, which has been facilitated by the development of a readily imaged matrix of collagen I (9,10,12,14,35). To this point, little work has been done to correlate a particular cell's migration or invasion with local structure of the matrix (though some such work is starting to emerge (5,6,36)), and much remains to be learned about the dual role of the ECM proteins in both facilitating migration by providing a tether point for integrins, but also potentially inhibiting migration by creating physical barriers for and exerting pressure on the cells.

This study examines GBM growth and invasion in collagen I matrices, on both the scale of the entire GBM system, and locally, at the tips of invasive cells. Imaging the entire GBM system with phase-contrast microscopy over several days provides evidence that specific cell-collagen fiber interactions are driving the tumor invasion and thus a microscopic analysis of matrix remodeling is crucial. This is particularly relevant because, as with collagen I matrices (37), the ECM environment in living tissues is grossly heterogeneous on length scales comparable to cell size. To visualize local matrix remodeling, we use confocal reflectance microscopy to image the collagen matrix simultaneously with coherent anti-Stokes Raman scattering (CARS) microscopy to image the invasive cells. Confocal reflectance microscopy (10,35,38) and CARS microscopy (39) have previously been used individually for cell biology studies, but have not previously been used simultaneously. These techniques are powerful and potentially applicable to a wide variety of biological problems as they provide three-dimensional microscopic resolution and do not require potentially perturbative fluorophores. Additionally, CARS is a chemically selective microscopy, as the contrast in a CARS image is due to narrow-band Raman active vibrations inherent to the sample. The examination of the GBM system at two length scales allows us to compare the role of ECM locally, as a crucial tether for cells during invasion, with its global role as a complex network that can either facilitate or inhibit GBM growth and invasion.

## EXPERIMENTAL PROCEDURE

### Preparation of glioblastoma spheroids

The human U87dEGFR glioblastoma cell line (40) was used to generate multicellular tumor spheroids (41). The cells were cultured in DMEM (Gibco Invitrogen, Carlsbad, CA) supplemented with 10% fetal bovine serum (JRH Biosciences, Lenexa, KS), 500  $\mu\text{g}/\text{ml}$  Geneticin Selective Antibiotic G418 (Gibco Invitrogen), 100 U/ml penicillin, and 100  $\mu\text{g}/\text{ml}$  streptomycin.

These cells will form irregularly shaped multicellular spheroids if they are allowed to become confluent. Spheroids of uniform size and shape can be formed by using the "hanging drop" procedure (42). Briefly, cells are incubated in a 10-cm tissue-culture dish for 3–6 days after the previous passage, the supernatant is aspirated, and 5 ml of Hanks' balanced salt solution (Gibco Invitrogen) is added. The supernatant is aspirated again, and 1 ml trypsin-EDTA (Invitrogen) is added. After several minutes of incubation, 9 ml of culture medium is added to neutralize the trypsin, and the mixture is transferred to a 50-ml conical tube. The cells are diluted to  $2.5 \times 10^4$  cells/ml with culture medium. Then, 20  $\mu\text{l}$  (500 cells) are dropped onto the inside cover of a 10-cm petri dish and the petri dish is filled with 10 ml culture medium. The dish is inverted and incubated for 3 days. The drops are held in place by surface tension, and the cells accumulate at the bottom of the droplet to form spheroids. Spheroids of  $\sim 200 \mu\text{m}$  in diameter are collected and placed into a collagen solution.

### Collagen matrix preparation

The collagen matrices are prepared from the following ingredients: a stock solution at 2.9 mg/ml collagen I (Vitrogen, Cohesion Tech, Palo Alto, CA), MEM 10 $\times$  solution (Gibco Invitrogen) and/or DMEM 1X solution (Gibco), 10% w/v sodium bicarbonate, fetal bovine serum (JRH Biosciences), penicillin/streptomycin (Gibco Invitrogen), and NaOH (1 N). Enough collagen is used to attain the desired final concentration (0.5–2.5 mg/ml), and 10% MEM, 100 U/ml penicillin, and 100  $\mu\text{g}/\text{ml}$  streptomycin are added. NaOH is added to bring the pH to 7.4, 2 mg/ml  $\text{Na}(\text{CO}_3)_2$  is added to buffer the gel, and the solution is topped off with deionized water to bring the total volume to 2.5 ml. The solution is well mixed and kept at 4°C, degassed for  $\sim 30$  min, and placed in one of three types of sample cells: 1-cm<sup>3</sup> plexiglass cubes, 1-cm diameter plexiglass cylinders of height up to 1 cm, or shorter ( $\sim 2$ -mm) glass chambers fully sealed with UV epoxy. In all cases, a thin glass coverslip forms the bottom of the sample cell. No differences were found in the structure of the collagen gels in the short versus the tall glass chambers, and the bare collagen experiments (experiments with no implanted cells) were done in the thin sample cells. Experiments on GBM in collagen matrices were done in the thick cubic or cylindrical cells in both anchored and relaxed gels. To prepare the sample cells to hold anchored gels, in which the collagen does not pull far from the walls as the solution gels and in which global remodeling by the cells is minimized, they are lined with nylon mesh to which the collagen anchors. For experiments in relaxed gels, no nylon mesh is used.

In the GBM/collagen samples, 400  $\mu\text{L}$  of collagen solution is added to the chambers. One to three spheroids are placed in each sample cell, and the sample cells are covered and incubated at 37°C and 5%  $\text{CO}_2$ . This begins polymerization of the collagen while maintaining the health of the cells. The MTSs generally sediment to the lowest 100–200  $\mu\text{m}$  of the sample cell, within the working distance of a typical high-numerical aperture objective. Full gelation occurs within 1 h, and a superlayer of culture medium is then added to maintain moisture and pH. The superlayer is changed at least every 48 h. In most cases, the spheroids remain healthy for 4–6 days. During brightfield and phase-contrast microscopy, the sample cells are in a temperature- and  $\text{CO}_2$ -controlled chamber. During confocal and CARS microscopy, the sample cells are on a temperature-controlled, but not  $\text{CO}_2$ -controlled, stage. Coverslips are affixed to the sample cells with mineral oil to prevent air exchange and help maintain pH during these measurements. Because the longest the samples were kept on the microscope stand during these types of microscopy was 3 h at a time, deleterious effects due to pH changes were not observed.

For the rheological measurements and some gel imaging in the absence of cells, collagen gels were prepared by mixing 1/10 volume of 10 $\times$  phosphate-buffered saline (PBS) with the appropriate volumes of stock 2.9 mg/ml collagen and deionized water. The pH was adjusted using 1 N NaOH. Gelation is induced by bringing the sample to 37°C. In confocal reflectance microscopy, this simpler collagen gel mixture is indistinguishable from the mixture prepared using DMEM.

## Rheology

The bulk elastic modulus of the collagen gels was measured using a stress-controlled rheometer (CVOR, Bohlin Instruments, Malvern, UK) with a 4°, 40-mm cone and plate geometry. The rheometer is equipped with a heating unit that allows us to maintain the sample at 37°C. The frequency-dependent elastic modulus,  $G'(\omega)$ , and loss modulus,  $G''(\omega)$ , were measured in the frequency range  $\omega = 0.1$ –5 Hz. We verified that the applied stress was sufficiently low to ensure the measurements were in the linear regime. In this frequency range, the mechanical response of all the networks probed is dominated by a nearly frequency-independent elastic modulus  $G' = G_0$ .

## Microscopy

To image the collagen matrix, confocal reflectance microscopy is employed (9,10,38,43). An Ar<sup>+</sup> laser at 488 nm is coupled into a Zeiss (Jena, Germany) LSM 510 Meta microscope through a fiber. An 80/20 reflecting beamsplitter is used to direct the light to the objective lens (63×, water; Olympus, Melville, NY). There is significant Rayleigh and Mie scattering from the relatively thick collagen I fibrils (44), which in part reflects the difference in index of refraction between the collagen fibrils ( $n \sim 1.4$ ) and the surrounding medium ( $n \sim 1.3$ ). The smallest fibril resolved is  $\sim 500$  nm, and the distribution of collagen fibril widths measured is in good agreement with the results of Brightman et al. (43), who further show that adding other ECM components to collagen I matrices does not have a profound effect on their structure. A confocal pinhole on the detection side allows for 3D resolution, and the pinhole is set to measure slices  $\sim 1$   $\mu$ m in depth along the optical axis. The reflectance signal returns through the 80/20 beamsplitter and is directed by a mirror through the confocal pinhole to a photomultiplier tube (PMT) detector (see Fig. 1).

To image the MTS and surrounding invasive cells, phase-contrast or CARS microscopy is used. Phase-contrast images are taken with a 5× objective lens (Leica, Heerbrugg, Switzerland) to monitor the MTS radius and the invasive distance defined by the cells radiating off the MTS. The MTS radius is the radius of the MTS, and the invasive distance is the radius of the entire GBM system minus the radius of the MTS (see Fig. 3 *d*). To take higher resolution images of the cells, CARS microscopy is employed. Confocal reflectance microscopy of the collagen and CARS microscopy of the cells are collected simultaneously (see Fig. 1). In some cases in which CARS and confocal reflectance are performed simultaneously, confocal reflectance is taken with the pump pulse (at 710 nm) from the CARS excitation instead of with the 488-nm laser to limit cell exposure to short wavelength light and to ensure excitation of the same  $z$ -position in the sample.

CARS is a nonlinear process that depends on the third-order susceptibility of a sample. Exciting a sample with two frequencies, a pump and Stokes frequency ( $\omega_p$  and  $\omega_s$ , respectively) chosen such that the frequency difference,  $\omega_p - \omega_s$ , is resonant with a Raman active vibration inherent to the sample, sets up a coherent oscillation of that resonant vibration in the sample. Interrogation of that excited superposition is achieved with a probe beam, here with the same frequency as the pump beam. This results in an inelastic scattering at a signal frequency,  $\omega_{\text{sig}} = 2\omega_p - \omega_s$ . Performing such a spectroscopy on a microscopic region requires high peak power and moderate average power, and is therefore achievable only when using pulsed lasers. CARS microscopy was first performed by Duncan (45) and more fully developed by Xie and others (46–49). Two titanium:sapphire oscillators (Coherent, Santa Clara, CA) are used to generate the pump and Stokes beams. These beams must be overlapped in both space and time at the sample. The time overlap is achieved via use of a Synchrolock system (Coherent) that continuously and precisely adjusts the cavity length of the slave laser to match that of the master laser. Thus, the pulse trains remain locked to each other with an average jitter of  $\sim 100$  fs (50). A collinear geometry is employed to achieve a compact point spread function; 3 ps pulses are employed, and the power at the sample is  $\sim 20$  mW for the pump beam and  $\sim 30$  mW for the Stokes beam. The pump (and probe) and Stokes

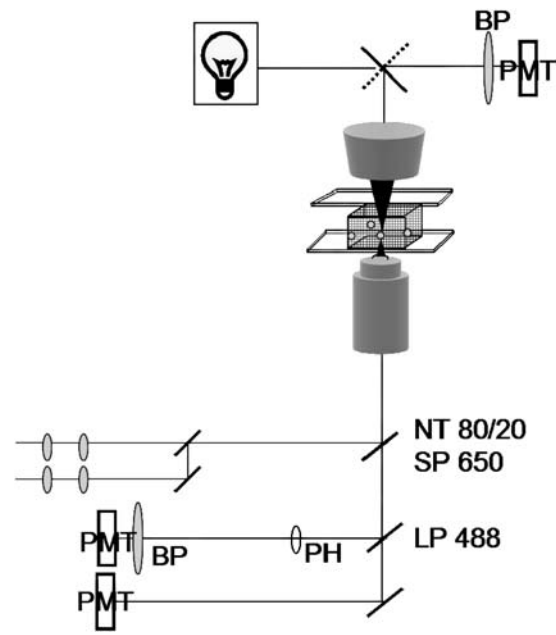


FIGURE 1 Microscopy setup. Collimated light enters the inverted scope and is directed to the objective by a beamsplitter (NT 80/20) for confocal reflectance, or a shortpass (SP) dichroic mirror (at 650 nm) for CARS. Light reflected from the sample passes through the beamsplitter, and is deflected by a longpass (LP) dichroic mirror (at 488 nm) through a pinhole (PH), bandpass filter (BP), and to a photomultiplier tube (PMT). CARS light is collected by the condenser in the transmitted direction and directed through a bandpass filter to a second PMT. A halogen lamp is used for brightfield images. Most transmitted light from the brightfield microscopy passes through the SP 650 and the LP 488 and is collected on a third PMT.

frequencies are set to be 14,085  $\text{cm}^{-1}$  and 11,240  $\text{cm}^{-1}$ , respectively. The frequency difference, 2845  $\text{cm}^{-1}$ , excites the CH<sub>2</sub> stretch in the cells. Because CH<sub>2</sub> bonds are exceedingly prevalent in the cell membrane and lipid droplets, these cellular entities give the most intense CARS signal for the pump and Stokes frequencies used here. For samples of thickness on the order of the wavelength or longer, phase-matching conditions dictate that the signal will be maximal in the forward direction at a wavevector ( $k$ ) defined by  $k_{\text{sig}} = 2k_p - k_s$  (48), and therefore the signal is collected in the forward direction. CARS microscopy is inherently confocal for the same reason that multiphoton fluorescent microscopy is: the intensity profile of the excitation volume is very sharp because it is defined by the intensity ( $I$ ) of the two frequencies employed as  $I_p^2 \times I_s$ , thus assuring there is little out of plane excitation.

Fig. 1 depicts the microscopy setup employed to simultaneously collect confocal reflectance and CARS images. The confocal reflectance images are measured in the reflected direction, whereas the CARS images are collected in the transmitted direction. Brightfield images can also be collected simultaneously with confocal reflectance images. The particular dichroic mirrors used are changed as appropriate. Fig. 2 *a* depicts a typical brightfield image of an invading GBM cell in a collagen matrix, and Fig. 2 *b* shows a typical CARS image of two invading cells. In addition to the benefit of 3D resolution afforded by CARS microscopy, the CARS image is clearly superior in revealing the cell morphology.

## Analysis of confocal microscopy images

To quantitatively ascertain the isotropy of the collagen gels imaged with confocal reflectance microscopy, several approaches are used. First, the

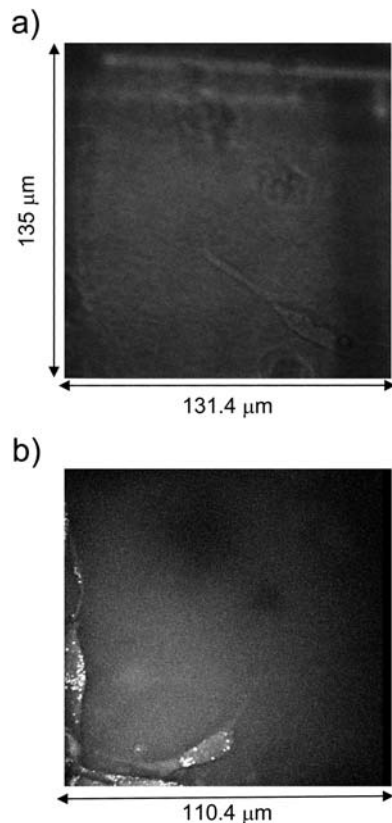


FIGURE 2 (a) Brightfield image of cells in a collagen I matrix. (b) CARS image of cells in the same collagen matrix.

number of collagen fibers that appear in each row and each column in 2D slices of the 3D collagen gel is determined. A pixel with intensity above a threshold (set so as to be above the intensity associated with background noise) is considered “on”, and the number of on-pixels per row and column are counted. The mean number of on-pixels for the rows and for the columns is defined, and the distribution around the mean is plotted. These are termed the row density distribution and the column density distribution, respectively. An isotropic system would be expected to have the same row and column density distribution. The distance between nearest neighbor on-pixels within each row and column defines a mesh size; the distribution of mesh sizes found for the rows and columns is plotted.

The second set of operations, analysis of fiber length and orientation distributions, provides necessary and sufficient proof of the presence of an isotropic matrix. Pixels greater than a certain threshold intensity that are connected to each other are identified. These pixels are then assumed to trace out a line between the minimum  $x$  coordinate,  $x_1$  (and its associated  $y$  coordinate,  $y_1$ ), and the maximum  $x$  coordinate,  $x_2$  (and its associated  $y$  coordinate,  $y_2$ ). Such a procedure does well in finding fibers in low-density matrices. To assist in location of fibers in high-density cases, a procedure to identify nodes is employed. This allows fibers that are branched or entangled to be identified independently. The identified fibers are analyzed in two ways: a histogram of the lengths of the identified fibers is plotted, as is a histogram of angles at which the fibers lie with respect to  $0^\circ$ , where  $0^\circ$  is defined by a line lying along a row and the positive (negative) angles are those lying above (below) the axis and range from  $0$  to  $(-90^\circ)$ . Because in the collagen matrices the fibers are  $>1$  pixel in width, the fibers that are found via the above procedure are unlikely to have  $x_1 = x_2$ . As a result, even in truly isotropic matrices, our procedure gives a histogram of angles of the identified fibers that is not flat across all angles but instead displays a spurious fall-off at angles approaching  $\pm 90^\circ$ .

## RESULTS AND DISCUSSION

### Global growth of GBM in collagen gels

To ascertain the growth of the glioblastoma multiforme spheroids in the Vitrogen collagen I matrices, the cells are placed in gels with collagen concentrations between 0.5 mg/ml and 2.0 mg/ml. The GBM spheroids are placed in two kinds of gels, anchored and relaxed, as described in the experimental section. Fig. 3 *a* shows the invasive distance of GBM spheroids as a function of collagen concentration over the first 12 h after implantation, Fig. 3 *b* shows the MTS radius of GBM spheroids as a function of collagen concentration over 94 h, and Fig. 3 *d* depicts how the MTS radius and invasive distance are defined. Each trace in Fig. 3, *a* and *b*, is derived from an average over four spheroids. (Two of these spheroids are in anchored gels and two are in relaxed gels. We find no qualitative or quantitative difference between the speed or pattern of growth in relaxed and anchored gels and thus average the results to generate the plots in Fig. 3, *a* and *b*. We do, however, note that 4 h after implantation, confocal reflectance images show that the relaxed gels appear to have a somewhat higher local density around the MTS, ostensibly reflecting a greater degree of remodeling of the relaxed gels in these first 4 h.) It is clear that over the first 12 h the spheroids in the two concentrated gels (1.5 and 2.0 mg/ml) invade more rapidly than do those in the less concentrated gels (0.5 and 1.0 mg/ml). This difference, however, does not persist for longer times, and by  $\sim 30$  h the invasive distances in the four types of gel are indistinguishable (not shown). Though the invasive distances of the GBM spheroids are similar after 30 h in all the gels, there is a striking difference in the pattern of growth of the GBM system in the low- and high-density collagen I gels as illustrated by Fig. 3, *c-f*. Fig. 3, *c* and *d*, show representative phase-contrast images of spheroids in 0.5 and 2.0 mg/ml 4 h after implantation, and Fig. 3, *e* and *f*, show representative spheroids at the same concentrations 24 h after implantation. After 4 h, the invasive distance of the GBM system and the number of invasive cells are greater in the 2.0 mg/ml gel than in the 0.5 mg/ml gel, as shown in Fig. 3, *c* and *e*, respectively. After 24 h, the difference in the invasive distances in the two gels has diminished, but the difference in growth pattern is even more pronounced, as shown in Fig. 3, *d* and *f*. In the 0.5-mg/ml gel there are relatively few invasive cells, and these cells tend to be invading along distinct branches (Fig. 3 *d*). On the other hand, there is such an accretion of invasive cells in the 2.0-mg/ml gel after 24 h that it is difficult to distinguish the MTS from the invasive cells (Fig. 3 *f*). These invading cells are not organized neatly into a few select branches but are invading everywhere. It is also of note that there are “rogue” cells in both gels at 24 h. These are cells that are part of neither the MTS nor any particular invasive branch; they do not appear to be connected to the MTS either directly or via a chain of invasive cells. These cells are typically rounder than other invasive cells. Because these cells are generally found at the periphery of the invasive area, they either moved faster on

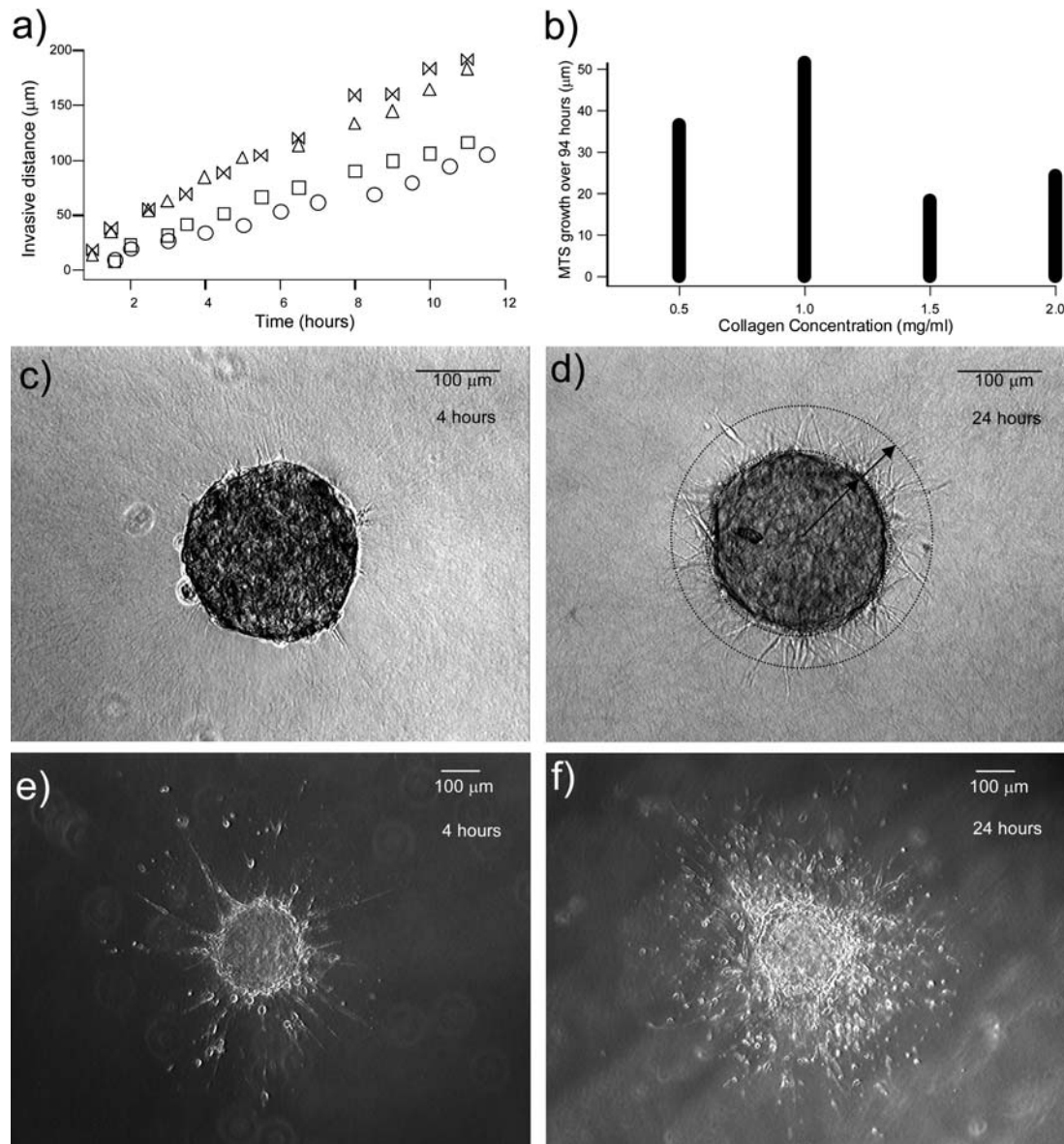


FIGURE 3 (a) Invasive distance of GBM in collagen I gels (0.5 mg/ml (○), 1.0 mg/ml (□), 1.5 mg/ml (△), and 2.0 mg/ml (▷◁)). (b) MTS growth over 94 h. (c) GBM 4 h after implantation in 0.5 mg/ml gel. (d) GBM 4 h after implantation in 2.0-mg/ml gel and definitions of invasive distance and MTS radius. The MTS radius is defined by the extent of the dense cells in the center of the GBM system. The invasive distance is defined as the distance between the periphery of the MTS and a circle that circumscribes the invasive cells. (e) GBM 24 h after implantation in 0.5 mg/ml gel. (f) GBM 24 h after implantation in 2.0-mg/ml gel. The contrast in *c* and *d* differs from that in *e* and *f* in that the former were taken with a 10× phase-contrast objective, whereas the latter were taken with a different (5×) phase-contrast objective.

average or started migrating earlier than other invasive cells. In addition to these cells at the periphery of the invasive distance, there are other rogue cells distributed throughout the invasive area. Indeed there are significantly more rogue cells in the 2.0-mg/ml gel at 24 h than there are in the 0.5-mg/ml gel. The occurrence of such single-cell migratory patterns is of interest clinically since it is well below the current resolution threshold of conventional imaging modalities used to diagnose and treat these tumors in patients.

The findings that over 12 h GBM MTS cells invade more quickly and that over all measured times they invade more

efficiently (in terms of numbers of invasive cells) in the higher-concentration gels, suggests that the number of available collagen fibers is a limiting factor in GBM invasion. Fig. 4, *a* and *b*, show confocal reflectance images of spheroids 3–4 h after implantation in anchored 0.5- and 2.0-mg/ml gels, respectively. Though confocal reflectance microscopy is chiefly employed to image the collagen fibers, it also captures aspects of the MTS. One-quarter of the MTS is visible in each of these images—in Fig. 4 *a*, the MTS is in the lower right-hand corner, in Fig. 4 *b* it is in the upper right-hand corner, and in Fig. 4 *c* it is in the lower left-hand corner. It is clear that there

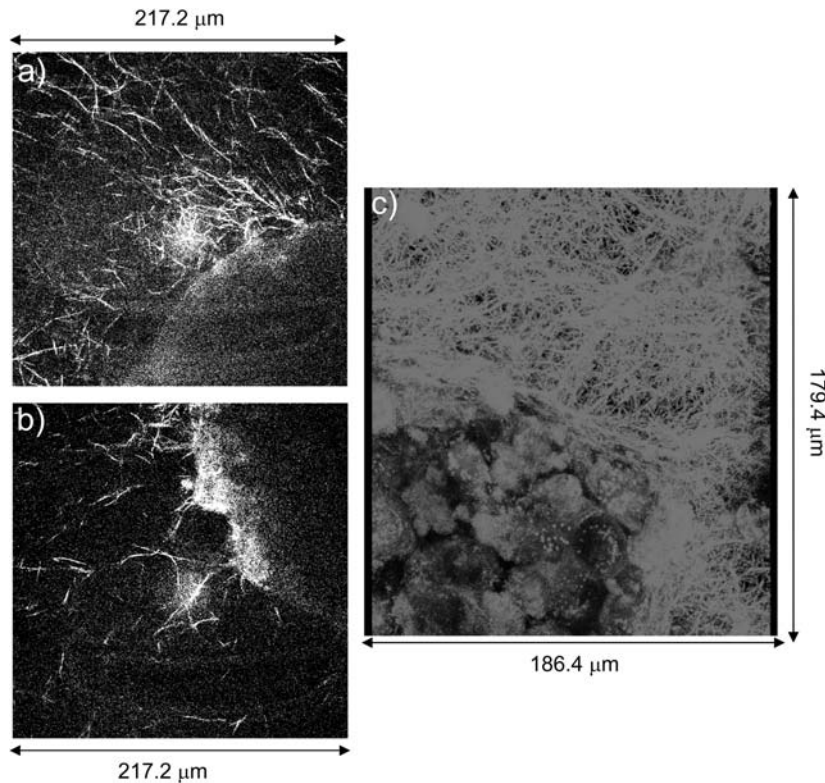


FIGURE 4 Confocal reflectance images of a quadrant of the MTS and surrounding collagen fibers 3–4 h after implantation. (a) MTS in a 2.0-mg/ml gel. (b) MTS in a 0.5-mg/ml gel. (c) Projection of confocal reflectance images of MTS in a 1.5-mg/ml collagen matrix several hours after implantation. Note the buildup of collagen around the edge of the MTS due to the growth of the MTS into the matrix.

are significantly more collagen fibers around the MTS in the 2.0-mg/ml gel (Fig. 4 *a*) than there are in the 0.5-mg/ml gel (Fig. 4 *b*). The number of collagen fibers around the MTS, then, is seen to strongly correlate with the number of invasive cells (Fig. 3, *c* and *d*).

Over all times measured (up to 94 h), the invasive distance in the 1.5-mg/ml gel is indistinguishable from that in the 2.0-mg/ml gel. One possible reason for this is that the high-concentration gels do not incorporate all the collagen into fibrils. This underscores the need for complementing our global examination of GBM growth and invasion in collagen gels with more detailed, local measurements. Indeed, the analysis of bare collagen gels presented in the next section reveals that the number of collagen fibrils per unit area revealed by confocal microscopy is the same in the 1.5- and 2.0-mg/ml gels. The extra collagen may be incorporated into smaller fibrils not resolved by confocal reflectance microscopy (51). If this is the case, it appears that these microfibrils neither help nor hinder GBM invasion. Another possible reason for the plateau of the speed of invasion in high-concentration gels was proposed by Gaudet et al. (16) to explain the spreading of fibroblasts on 2D collagen I surfaces. They propose that a plateau in the amount of spreading on 2D surfaces of increasing collagen concentration is caused by the finite number of cell integrins. A direct comparison to Gaudet's results is not possible for several reasons: they use a 2D substrate with unknown microscopic structure, whereas we use a 3D matrix with thick collagen

fibrils. Further, whereas fibroblast cells are reported to have  $\sim 200$  integrins/ $\mu\text{m}^2$  (16), to the best of our knowledge the number density of integrins on actively invading GBM cells has not been reported. Because the local collagen concentration around the spheroid in the high concentration gels is so high, it is plausible that these cells are in an environment where all the integrin receptors are engaged, and further increases in fiber density do not yield any increase in integrin-mediated motility. The plateau could also have a more basic, physical explanation: collagen fibers and/or microfibrils may be forming too dense a physical barrier for invasion to occur efficiently. Our microscopic studies indicate that GBM invasive cells generally exhibit mesenchymal motion and do not squeeze through small spaces in the ECM. Thus, the physical barrier created by the fibrils may indeed effect the plateau in invasive speed and numbers of invasive cells in high-collagen concentration gels.

Although invasive distance growth only correlates with collagen concentration over the first 12 h after implantation, it is only after several days that MTS radius growth appears to correlate with collagen concentration. By 80–100 h after implantation, the MTSs have grown less in the high-concentration gels than in the low-concentration gels (Fig. 3 *b*). One potential factor in the relative slowness of the MTS growth at high concentrations is the pressure exerted on the MTS by the collagen accumulating around it. Sufficiently high pressures have been shown to effectively stop tumor growth (52). Fig. 4 *c* is a projection of the collagen matrix

around the MTS in a 1.5-mg/ml gel 4 h after implantation. As the MTS grows, the collagen in the surrounding matrix bunches up against the MTS. As will be shown in the next section, such an agglomeration of collagen fibers will make the gel in this region locally more elastic, or stiffer. To grow volumetrically into this stiff area of the gel, the MTS would need to exert greater force than was required to grow into this same gel at early times, before collagen congestion around the MTS became significant.

The main results from the phase-contrast microscopy of the entire GBM system are that early invasion speed correlates positively with collagen concentration, that MTS growth is slowed at high collagen concentration, and especially that high collagen concentration correlates with a higher number of invasive cells. These results demonstrate that environment microstructure and mechanical properties should be considered in studying GBM invasion and lead us to investigate cell migration on a shorter length scale, where we can concentrate on the interaction of the invasive cell tips and collagen fibers.

### Microscopic structure of bare collagen gels

As a control and a necessary first step in understanding how GBM cells remodel collagen I matrices, collagen gels of various concentration ( $c = 0.5\text{--}2.5$  mg/ml) are examined in the absence of cells. We study these gels both globally, with bulk rheology, and locally, with confocal reflectance imaging. Bulk rheology experiments on these collagen gels reveal that the elastic modulus of the gels is approximately an order of magnitude greater than the viscous modulus, showing that even the weakest of these gels behaves primarily as an elastic solid. The elastic modulus of the 0.5-mg/ml gel is 4 Pa, that of the 1.0 mg/ml gel is 11 Pa, and that of the three most concentrated gels (1.5, 2.0, and 2.5 mg/ml) is  $\sim 100$  Pa. For comparison, the elastic modulus of Jello is  $\sim 100$  Pa, whereas that of brain tissue is  $\sim 50$  Pa at 1 Hz, (53). The plateau in elastic modulus at  $c > 1.5$  mg/ml suggests that the extra collagen may not be incorporated into the load-bearing collagen network and is consistent with the finding that the GBM system has similar growth and invasion profiles in the 1.5- and 2.0-mg/ml matrices.

Detailed rheological measurements will be reported in a future publication (C. P. Brangwynne, E. Filippidi, K. E. Kasza, L. J. Kaufman, and D. A. Weitz, unpublished); however, several points revealed by the bulk rheology are worth mentioning here. As has been shown previously (54), collagen gels at  $c \geq 1.0$  mg/ml strain stiffen at  $\gamma \geq 0.1$ . The strain stiffening may be related to alignment of the collagen fibrils or subunits therein. Both the elastic modulus and strain stiffening seen in the higher-concentration gels is quite similar to that reported in brain tissue (53,55), suggesting that the collagen I matrix is, from a mechanical standpoint, a reasonable model for the in vivo environment of GBM. Interestingly, after being submitted to strains of  $>0.1$ , the elastic modulus ( $G'$ ) is lower than that of the initial gel. This

suggests that although straining the system may lead to fiber alignment, it may also break weak links in the gel, leading to the lower initial elastic modulus observed.

Collagen matrices at four of the concentrations (0.5, 1.0, 2.0, and 2.5 mg/ml) at which bulk rheology was performed are imaged with confocal reflectance microscopy in Fig. 5. A visual inspection suggests that the matrices are isotropic and that the average mesh size as a function of concentration ( $\xi(c)$ ) goes as  $\xi(.5) > \xi(1) > \xi(2) \sim \xi(2.5)$ . These images are taken  $\sim 30$   $\mu\text{m}$  into the sample, and no significant differences in fiber density or isotropy within a matrix of a particular concentration are seen over the first 250  $\mu\text{m}$  of the matrix (the working distance of the objective). Fig. 5 *b* contains both the confocal reflectance image as well as red lines drawn over the fibers identified via the procedure described in the experimental section. This is a representative depiction of how well the fiber-location algorithm performs in the gels studied. Fig. 6 displays the normalized results of the analysis for the 0.5-, 1.0-, and 2.0-mg/ml gels. The 2.5-mg/ml gel gives results similar to the 2-mg/ml gel and is not included on these graphs. Fig. 6 *a* shows that the total (sum of row and column) mesh size distribution exhibits an exponential decay over three to five decades. This is expected in a random array, where the location of a fiber that defines a mesh is not dependent on the location of other fibers. For all three gel concentrations, the mesh size distribution for the rows quantitatively overlays that for the columns (not shown), also expected in an isotropic system. Fig. 6 *a* shows that the mesh size of the sample decreases as the concentration increases. The characteristic mesh sizes are determined by fitting the mesh size distribution to an exponential decay. This procedure gives  $\xi = 27.8, 12.1, \text{ and } 8.3$   $\mu\text{m}$  for the 0.5-, 1.0-, and 2.0-mg/ml gels, respectively.

In a 3D system of random, moderately inflexible rods, one expects the density,  $\rho$ , to scale with  $\xi$  as  $\rho \propto (1/\xi^2)$  (56). Because the system is expected to be isotropic in  $x, y, \text{ and } z$ , examining 2D slices of a 3D network does not change the expectation for the measured mesh size dependence on concentration assuming that the  $z$ -resolution is good compared to the mesh size (as it is in these gels). Since the mesh size of the 2-mg/ml gel is 8.3  $\mu\text{m}$ , that of the 1.0-mg/ml gel would be expected to be 11.0  $\mu\text{m}$  and that of the 0.5-mg/ml gel would be expected to be 16  $\mu\text{m}$ . So, the 0.5-mg/ml gel has a mesh size significantly greater than that predicted by  $\rho \propto (1/\xi^2)$ . We propose that this effective repulsion between the fibers at low concentration may be related to the discrepancy between the amount of collagen needed to nucleate fibril formation versus that needed to allow for fibril extension. In some areas of low collagen concentration matrices, there may not be sufficient collagen for fibril nucleation but there may be sufficient collagen to lengthen an existing fibril. This would lead to a local depletion of collagen fibrils and a larger mesh size than predicted by simple scaling arguments. The inset of Fig. 6 *a* shows mesh size (*left axis, circles*) and the bulk elastic modulus (*right axis, squares*) as a function of concentration.

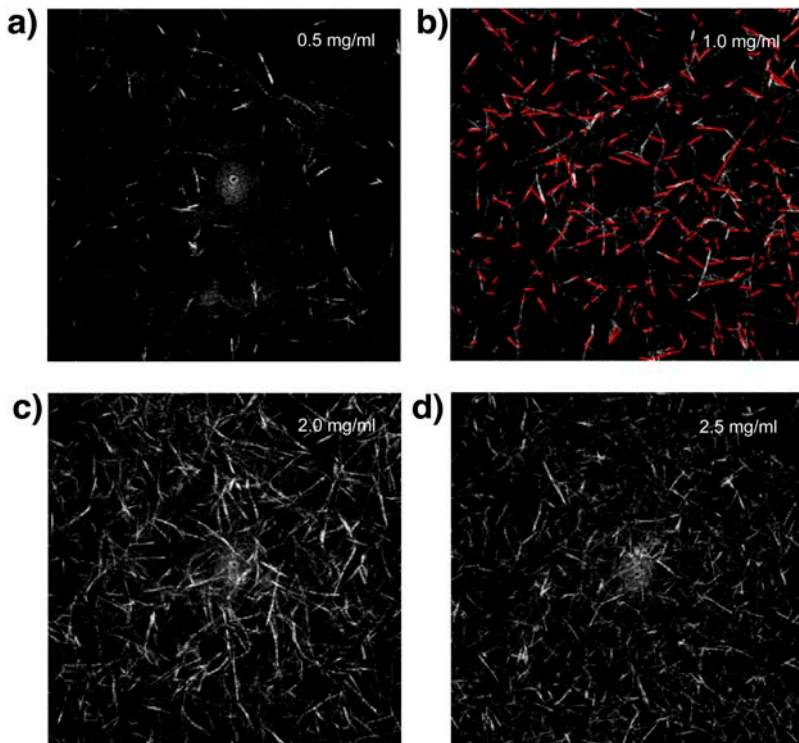


FIGURE 5 Confocal reflectance images of four collagen matrices: (a) 0.5 mg/ml; (b) 1.0 mg/ml; (c) 2.0 mg/ml; and (d) 2.5 mg/ml. All images are  $153.6 \times 153.6 \mu\text{m}$ . Panel b contains both the confocal reflectance image and red lines overlying the collagen fibers identified by the analysis procedure employed. Some pixels in the center of the image are removed to eliminate speckle from the image.

A variety of models have been proposed for how  $G'$  scales with concentration (57,58). In simple models for high-porosity gels, the prediction is  $G' \propto \rho^2$  (58). For our gels,  $G'$  decreases with decreasing density faster than  $\rho^2$ , and the  $\rho$ -dependence cannot be well fit by a power law. The deviation from the simple scaling could again be explained by the hypothesis presented above. Indeed, the fact that the collagen matrices do not follow simple scaling models for either mesh size or elastic modulus with concentration emphasizes that the collagen network is more complex in both structure and formation than a network of rods or semiflexible polymers. This contrasts with other biopolymers, such as actin (59), that show better agreement with the scaling of such simple models.

Fig. 6 b shows the row and column density distribution for the three gels. In all cases the row density distribution overlaps well with the column density distribution (not shown), as should be true of an isotropic array. The distributions all have a tail on the high-density side of the distribution, and when not normalized by the mean density, are moderately well fit by Poisson distributions (not shown), as should be the case in a random system. The  $\rho$  distribution of the 0.5-mg/ml gel is quite narrow compared to that of the 1.0- and 2.0-mg/ml gels. This suggests that the fibers are rather far apart from each other and very evenly distributed. This is not unexpected of a low-concentration collagen gel, which by definition must have its relatively few constituent fibers span the system.

The second portion of the analysis of the 2D slices of the 3D collagen matrices involves associating sets of on-pixels with lines and then analyzing their length and angular distribution.

The characteristic length of unbranched portions of the fibers in a plane of  $\sim 1 \mu\text{m}$  thickness is extracted from an exponential fit to the distribution of collagen fiber lengths (Fig. 6 c). This characteristic length is found to grow linearly with increasing collagen concentration, from  $2.1 \mu\text{m}$  for the 0.5-mg/ml gel to  $3.7 \mu\text{m}$  for the 2.0-mg/ml gel, as shown in the inset of Fig. 6 c. In the lowest concentration gel, the characteristic length is  $\sim 1/10$  the average mesh size, whereas in the stiffest gel studied, the characteristic length is  $\sim 4/10$  the average mesh size. The trend in characteristic length perhaps reflects a greater ability of the fibers to grow out of the plane where the network is sparse. Finally, in Fig. 6 d, the angular distribution of the identified fibers is displayed. All gel concentrations have a fairly flat distribution, again emphasizing the isotropy of these gels within the plane in the absence of cells.

### Matrix remodeling by individual cells

To quantify how a glioma system remodels the collagen matrix as invasive cells move away from the MTS, we perform the same analysis on remodeled collagen matrices as we do on the bare collagen matrices presented above. First, we discuss basic aspects of GBM growth and invasion as revealed by high resolution CARS images of GBM growth in collagen I matrices. Fig. 7 shows growth of the MTS and the invasion of cells at its periphery. Significant growth in the  $\sim 3$  h over which these CARS images are collected is evident. Notably, early branches defined by invasive cells are subsequently filled by larger, rounder cells that are part of the MTS. Thus,

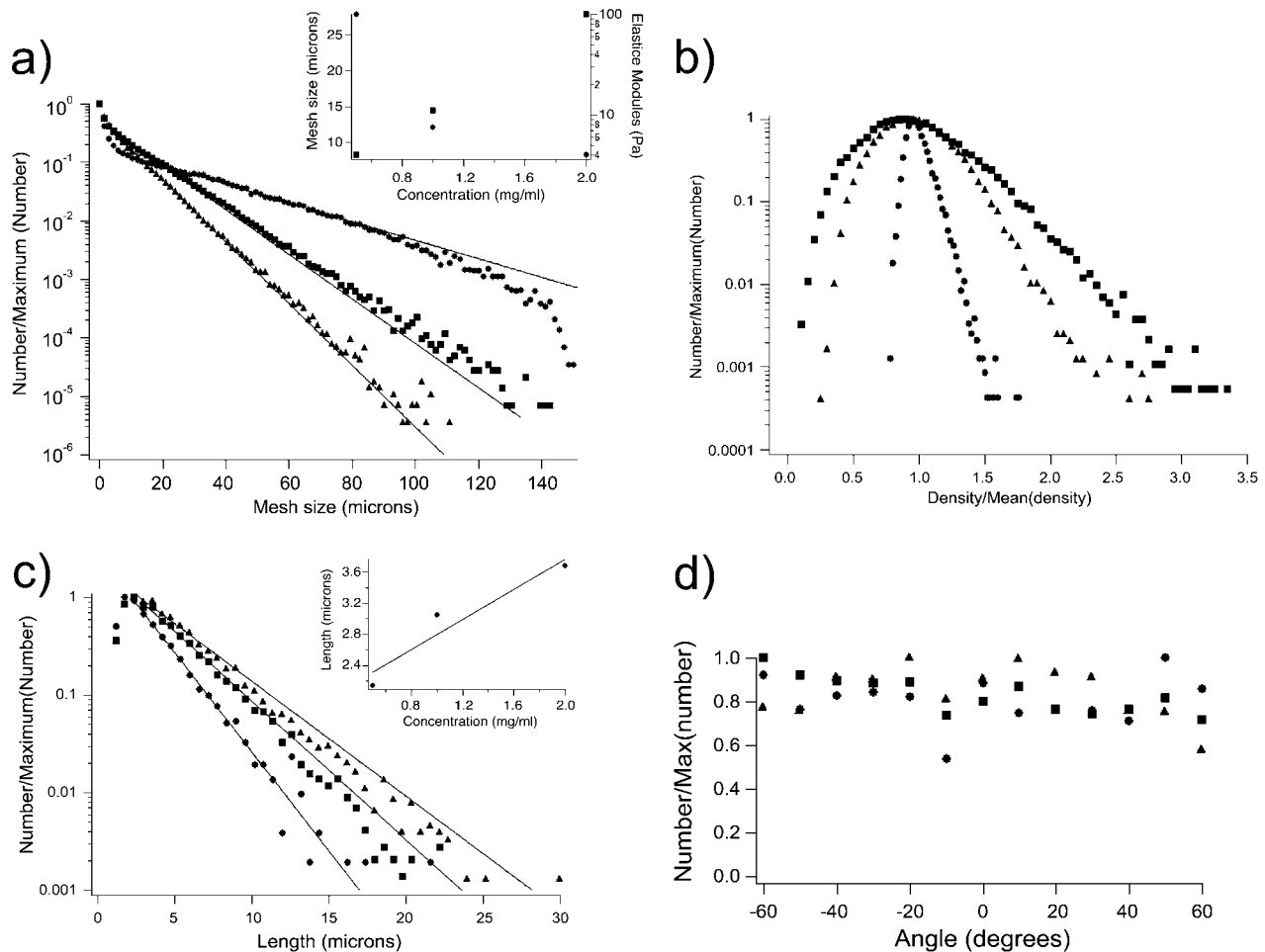


FIGURE 6 (a) Mesh-size distribution for 0.5 mg/ml (●), 1.0 mg/ml (■), and 2.0 mg/ml (▲) bare collagen gels with exponential fits. (Inset) Mesh size (●, left axis) and elastic modulus (■, right axis) as a function of concentration. (b) Row density distribution (see text for details) for 0.5 mg/ml (●), 1.0 mg/ml (■), and 2.0 mg/ml (▲) bare collagen gels. (c) Histogram of lengths of fibers identified via the procedure illustrated in Fig. 5 *b* for the 0.5-mg/ml (●), 1.0-mg/ml (■), and 2.0-mg/ml (▲) bare collagen gels and fits to exponentials. (Inset) Characteristic fiber length versus concentration. (d) Angular distribution from  $-60^\circ$  to  $60^\circ$  for the 0.5-mg/ml (●), 1.0-mg/ml (■), and 2.0 mg/ml (▲) bare collagen gels.

not only do invasive cells follow the path of least resistance laid down by the leading invasive cells (60), but the proliferative MTS also preferentially expands into these areas first. The cells that define an invasive branch are rather elongated. The leading edge of the leading invasive cell has many cell protrusions that colocalize with collagen fibers. There is slow forward motion of the cell, during which a cone of collagen fibrils is collected by the invading cell. After the restructuring of the collagen fibrils into a cone, the cells partially retract their pseudopodia and move back, and the cone of collagen fibers is pulled toward the MTS. Because local remodeling of the matrix occurs during both the forward and backward movement of the cell, the invasive cells appear to exert traction during both the accumulation of the collagen and the partial retraction of the pseudopodia, during which the collagen is pulled toward the MTS. This is in agreement with the findings of Roy et al. (23) for fibroblasts on a 2D collagen matrix.

For cells to continue moving forward after one cycle of extension and partial retraction of pseudopodia, the cells must either change direction, release the collagen fibrils, or degrade the collagen fibers in their path. There is no evidence for the cells changing direction; instead, the evidence suggests significant persistence of motion in a particular direction. We also note that our time lapse images show no evidence for degradation of significant quantities of collagen, likely because any such degradation will occur at shorter length scales and in smaller amounts than can be resolved with optical microscopy. It is known, however, that gliomas produce MMPs (61–65), and these enzymes have been implicated in a wide range of behaviors including the breakdown of ECM, early carcinogenesis events, tumor growth, and metastasis (65). To ascertain whether MMPs are at play in our *in vitro* model (as well as whether our *in vitro* model is a reasonable one for understanding GBM growth and invasion *in vivo*), assays that detail MMP activity must be performed. That may include, for

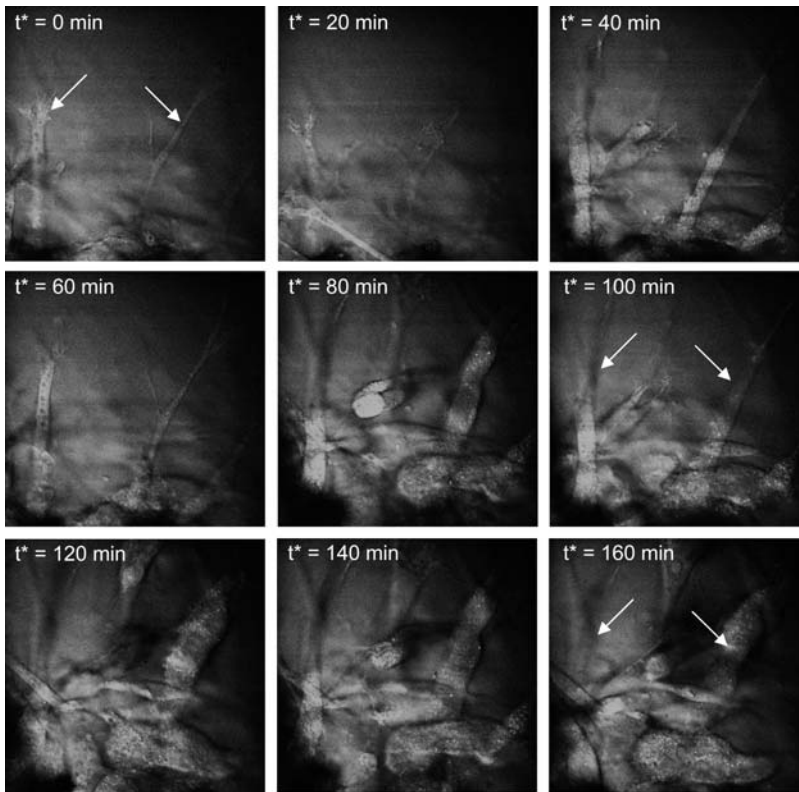


FIGURE 7 CARS images at the periphery of the MTS taken 20 min apart. All images are  $97.2 \mu\text{m} (x) \times 95.7 \mu\text{m} (y)$ .  $t^*$  is the time elapsed from the beginning of the observation time,  $\sim 3$  h after implantation. Arrows point to two particular cells at  $t^* = 0, 100,$  and  $160$  min to show that paths initially filled with thin invasive cells are later filled with thicker proliferative cells.

instance, experiments in which MMP activity can be up- or downregulated in the particular cell line used (66).

As the cell continues its motion, it retracts, taking the cone of collagen fibers with it. The cell then partially releases the collagen it has collected, and the highly anisotropic local collagen environment relaxes to a certain extent. The partial persistence of the concentration of collagen fibers allows the cell an uncongested, but collagen-populated, area for the next step in the migratory cycle. Matrix remodeling seen during one of these cycles is shown in Fig. 8 and a supplemental movie. Fig. 8 *a* shows an image of the collagen fibers at time 0 (defined by the beginning of the observation, several hours after spheroid implantation) subtracted from an image taken at the same location 40 min later. The cell's position, as measured with CARS microscopy, but not included in the figures for clarity, is shown by the dotted line, with the extension beyond the frame pointing toward the MTS. The original images are filtered with a bandpass filter, so that the differences seen are due not to pixel-pixel variation, but to larger-scale motion of the collagen fibers. Although the fibers are rather isotropic at time zero, they have assumed a triangular form extending from the end of the cell to the left top and bottom corners of the image frame by the time the second image shown is acquired. Taking a stack of  $xy$  images of this area (not shown) shows that the fibers do trace out a 3D cone extending from the tip of the cell. Fig. 8 *b* depicts the matrix remodeling between minutes 40 and 72: during this time the cone of fibers persists and moves in toward the MTS. This

occurs as the cell processes partially retract and the cell moves back. A supplementary movie is included to clarify these steps of glioma cell migration and matrix remodeling. The movie consists of 18 frames taken 4 min apart and depicts the cell collecting and pulling on the collagen fibers before moving forward. Fig. 8 *c* shows an image taken at 72 min subtracted from one taken at 146 min. Partial relaxation of the matrix (not shown in the supplemental movie), with the fibers diverging from the cone and creating a more isotropic matrix, is evident by 2.5 h after the beginning of the observation time. It is clear that in this case,  $\sim 2.5$  h after the onset of reorganization of the collagen matrix by this invading cell, the path directly in front of the cell is moderately clear, but does include collagen fibers onto which the cell could exert traction if this cell were to continue to move in the same direction it did in this cycle.

Taking the example of matrix remodeling shown in Fig. 8 and the supplemental movie, a strain exerted by the cell on a particular fiber or small number of fibers can be estimated. In one particular case that is representative of the behavior of the collagen fibers during remodeling, as the cell moved over  $\sim 25 \mu\text{m}$ , a fiber was stretched from a bent or branched configuration with total contour length of  $27.4 \pm .5 \mu\text{m}$  to an extended configuration with length of  $29.6 \pm .5 \mu\text{m}$ . In this case, the strain on that particular fiber is  $\sim 0.08$ . From these same measurements, we can also estimate  $\gamma$  in the networks by measuring the distance moved during remodeling by several points on several collagen fibers. The technique we use is complementary to the use of polarized light

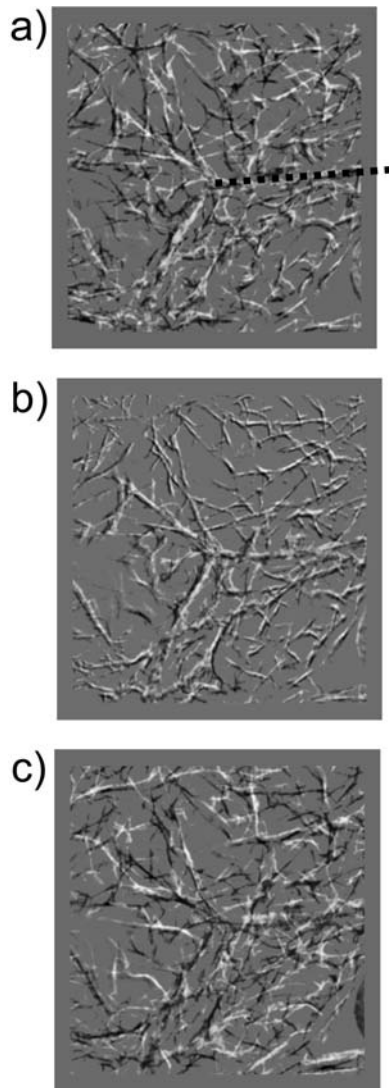


FIGURE 8 Confocal reflection images of collagen fibers subtracted from images of the same location at a later time. All images are  $179.4 \times 179.4 \mu\text{m}$ . The difference images have negative (*black*) and positive (*white*) components, and thus the black portions of the images correlate with the early time fiber arrangement whereas the white portions of the images correlate with the fiber arrangement at the latter time point. (a) Time zero (defined by start of the observation time) and time 40 min. Dotted line indicates the location of the cell. (b) Minute 40 – minute 72. (c) Minute 72 – minute 146.

microscopy to determine strain fields in a gel as first applied in a quantitative manner by Tranquillo and others (67). Although polarized light microscopy measures bulk strain on a gel matrix, it does not allow measurement of how one cell can affect one fibril or, therefore, measurement of the heterogeneity of the network deformation. For the matrix depicted, we measure a wide distribution of distances traversed by the collagen fibers, though the average for the fibers shown is  $\sim 1 \mu\text{m}$ . This matrix is a 1.5-mg/ml gel, expected to have a mesh size of  $\sim 10 \mu\text{m}$ , giving a strain of  $\sim 0.1$ . These two methods of calculating strain give a result that is comparable to the critical

value of 0.1 strain at which bulk rheology shows that the system both strain stiffens and also has components that break. The strain stiffening is presumably associated with the alignment of fibers seen in the confocal reflectance images of remodeled matrices. The components that break, leading to the weaker initial elastic modulus after submission to high strains, may be occurring on a much shorter length scale, as we see no evidence for broken collagen fibers in the confocal reflectance images. The fact that the matrix strain stiffens may be important because this stiffening can create a positive feedback cycle encouraging the cell to continue to move in that direction, as cells have been shown to move toward more rigid portions of 2D substrates and exert more traction on the more rigid substrates (16,18,21,68). In addition, the fact that strains on the order of 0.1 seem to disrupt finer components of the collagen matrix, resulting in lower linear elastic moduli, suggests that the cells may be mechanically weakening the matrix on microscopic length scales simply by pulling on it. This weakening may allow the reorganization of the matrix around the cell tip to occur more easily and may also assist in deadhesion at the integrin receptors after partial cell retraction. Although this does not per se exclude a role for MMPs in weakening the matrix (yielding enhanced cell migration), it does suggest that purely mechanical activity can contribute to that weakening.

One way to estimate the forces exerted by the cells as they deform the network over a given distance is to approximate the network response as linear elastic and obtain a spring constant using  $G'$  and a pertinent length scale, which is chosen to be  $\xi$ , the mesh size. Then,  $F = G' \xi \Delta x$ . While cells are exerting traction, the displacement of the fibers ( $\Delta x$ ) is typically  $1 \mu\text{m}$  and infrequently  $>2 \mu\text{m}$ . Using  $\Delta x = 1 \mu\text{m}$  gives forces of 100 pN for the 0.5-mg/ml gel, 130 pN for the 1.0-mg/ml gel, and 800 pN for the 2.0-mg/ml gel. The measured forces are consistent with those measured previously: for example, Roy finds that corneal fibroblasts exert traction forces of  $\sim 2 \text{ nN}$  on a 2D collagen substrate (23), whereas Meshel et al. (32) find that NIH-3T3 fibroblasts exert forces between 180 and 250 pN on an individual collagen fiber in a 3D matrix.

Over times up to 1.5 h, the speed of the leading invasive cells varies from  $0.25 \mu\text{m}/\text{min}$  to  $0.8 \mu\text{m}/\text{min}$  during both extension and partial retraction. In this set of experiments, speed was measured in 12 cells, all in anchored matrices at either 0.5 or 1.5 mg/ml. We have not observed sufficient cells to have statistically meaningful results for the speed at each concentration; however, it is notable that two invading cells measured simultaneously in one 0.5-mg/ml anchored matrix were at the extremes of the measured speeds, demonstrating that there is a significant distribution of cell speed within a matrix of a particular concentration. Over 10–12 h, the measured speeds are higher than the average speeds determined from the slopes of the data in Fig. 3 *a*. This is because these results average over times during which cells are not moving forward. The average individual cell speed

(0.25–0.8  $\mu\text{m}/\text{min}$ ) is in good agreement with previous measurements, though none are in systems fully comparable to that studied here. Chicione et al. (69) find that malignant astrocytomas plated with feeding medium have an average velocity over 2 h of 0.21  $\mu\text{m}/\text{min}$ . Roy et al. (23) find that corneal fibroblasts plated on collagen I travel with an average speed of 0.12  $\mu\text{m}/\text{min}$ . Lo et al. (18) find fibroblast speed to be 0.26–0.44  $\mu\text{m}/\text{min}$  on moderately rigid 2D substrates of collagen I, whereas Gaudet et al. (16) find cell speed to be between 0.07 and 0.17  $\mu\text{m}/\text{min}$  on substantially less stiff substrates.

Fig. 9, *a* and *b*, show two cells attached to the MTS that have effectively remodeled the collagen matrix via the same set of steps depicted in Fig. 8 and the supplemental movie.

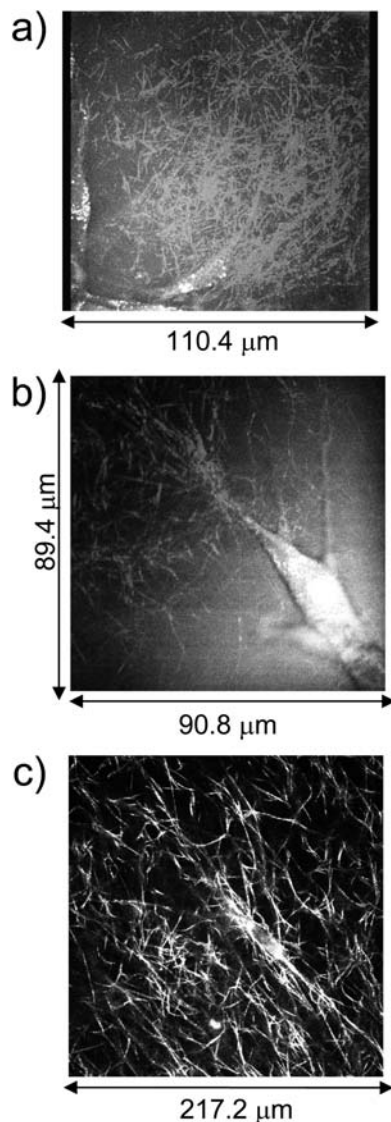


FIGURE 9 (*a* and *b*) Confocal reflectance images of remodeled collagen matrices superimposed with simultaneously collected CARS images of invasive cells attached to the MTS. (*c*) Confocal reflectance image of remodeled collagen matrix and cell detached from the MTS.

Fig. 9 *c* shows a cell that is not attached to the MTS that retains the same general shape as the attached cells and also has effectively remodeled the matrix. The confocal reflectance image of the collagen fibers and the CARS image of the cell (Fig. 9, *a* and *b* only) are recorded simultaneously. In all cases there is significant colocalization of the tip of the cells and the collagen fibers. A *z*-stack of images (not shown) of the cell in Fig. 9 *b* reveals that there is a cone of fibrils present as in Fig. 8. Examining the cell image without the superimposed confocal reflection image of the collagen reveals that the cell tip has many small pseudopodial extensions. In Fig. 9, *a* and *c*, clustering of the collagen is evident not only at the tip of the cell, but also along its sides. This may occur as a cell remodels the matrix and then moves along one of the edges of the cone of fibrils it had collected in previous cycles. Matrix remodeling of this type would be very effective in laying down a track for subsequent invasive cells to follow. This would be further aided by paracrine activity, since under specific conditions, GBM cells have already been shown to be capable of producing ECM fibers themselves (70).

Analyzing a *z*-stack of images collected 25  $\mu\text{m}$  above and below the cell displayed in Fig. 9, *b* and *c*, in the same way that the bare collagen matrices were analyzed allows us to quantify several differences between bare collagen matrices and remodeled ones. Fig. 9 *b* shows an invasive cell attached to the MTS. The cell is oriented at an angle of  $\sim 45^\circ$  with respect to a line along a row. Fig. 10 *a* shows that the row and density distributions differ significantly from each other, as would be expected in an anisotropic system. In addition, each of the density distributions varies significantly from the Poisson distribution expected in an isotropic matrix and seen in the bare collagen matrices. The density distributions in the remodeled matrices tend to be bimodal and very wide compared to density distributions of bare collagen gels of the same concentration. Both the bimodality and width of these distributions reflect the clustering of collagen fibers near the tip of the cell, i.e., there is a very high density of fibers around the tip of the cell and there are low density areas elsewhere. The mesh-size distribution of the matrix in the area of the tip and the 25  $\mu\text{m}$  above and below the cell into which the cone of fibrils extends can only be well fit to an exponential over part of the range of mesh sizes (not shown). The fit to the exponential fails at both small and very large mesh sizes, as is expected since the remodeled matrix shows many anomalously small and large pores compared to the bare matrix. The histogram of angles of the remodeled matrix shows that it differs significantly from an isotropic matrix as well, and indeed is broadly peaked around an angle close to that at which the cell lies. Fig. 10, *c* and *d*, shows the same analysis for the cell pictured in Fig. 9 *c*. The results for the density and mesh-size distributions are similar for the remodeled matrix surrounding this detached cell and that surrounding the attached invasive cell. Indeed, this cell has remodeled the matrix significantly over a volume of  $217 \times 217 \times 50 \mu\text{m}$ . This result shows that cells detached from the

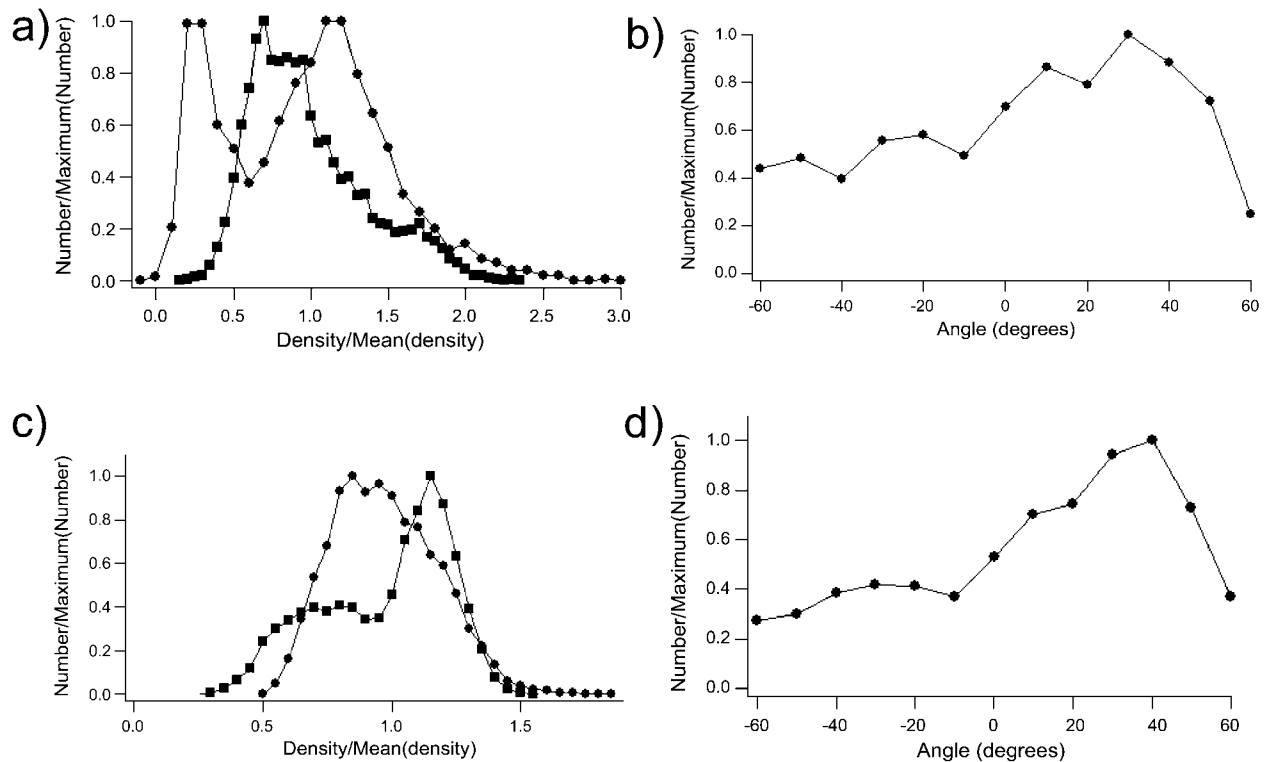


FIGURE 10 (a) Row (●) and column (■) density distributions for the 1.5-mg/ml remodeled matrix shown in Fig. 9 *b*. (b) Angular distribution from  $-60^{\circ}$  to  $60^{\circ}$  for the 1.5-mg/ml remodeled matrix shown in Fig. 9 *b*. (c) Row- (●) and column (■)-density distributions for the 1.5-mg/ml matrix shown in Fig. 9 *c*. (d) Angular distribution from  $-60^{\circ}$  to  $60^{\circ}$  for the 1.5-mg/ml remodeled matrix shown in Fig. 9 *c*.

MTS (and not receiving chemical or mechanical signals predicated on cell-cell attachment) can remodel the matrix and in fact impact the microenvironment far beyond the scale of the size of the cell body. Our results, therefore, strongly support the importance of cell-matrix interactions for tumor cell invasion.

## CONCLUSION

Employing a variety of techniques, including bulk rheology, phase-contrast microscopy, and the novel simultaneous use of confocal reflectance and CARS microscopy, allowed us to study both bare collagen matrices and those with implanted GBM cells on two length scales. For the bare collagen matrices, bulk rheology allowed study of the strength and elasticity of the gels, whereas confocal reflectance microscopy allowed us to correlate those quantities with microscopic structure. The collagen matrices with implanted GBM multicellular tumor spheroids were studied on the length scale of the entire tumor system with phase-contrast microscopy, and on a shorter length scale, to examine details of the glioma cell-collagen interactions, using simultaneous imaging of the matrix by confocal reflectance microscopy and of the live cells by CARS microscopy, both of which provide three-dimensional resolution and neither of which require labeling

with fluorophores. Our major findings are that GBM tumors are affected significantly by the total collagen concentration in the gel, and there are distinct growth patterns in low- and high-concentration collagen I gels. Specifically, increasing concentrations of collagen I correlate positively with invasion, but negatively with MTS growth. Further, these measurements suggest that available collagen fibers and/or integrins are a key determining factor in the number of invasive cells. Examination of bare collagen gels shows that they are isotropic, and our analysis provides necessary and sufficient evidence to show this. Finally, monitoring local remodeling of the matrix by the lead invasive cells reveals that 1), these glioma cells exhibit largely mesenchymal movement; 2), they travel forward and backward at speeds between 0.25 and 0.8  $\mu\text{m}/\text{min}$ ; 3), the forces exerted during traction are on the order of 100 pN and can be upregulated with increasing collagen concentration; 4), the cells strain the matrix sufficiently to cause both strain stiffening and breakage of certain components of the gel; and 5), attached and detached cells remodel the matrix significantly in a way that can be quantified by looking at the density and orientation of collagen fibers in the vicinity of the invasive tips. Of these results, one of the most important is that the cells, through the mechanics of migration, change the surrounding matrix sufficiently to align it, strain stiffen it, and break certain

components in it. Such findings stress the importance of considering the mechanics of cell migration alongside the biochemical aspects involved in migration. Although the findings on the importance of mechanics in migration are likely to generalize to most migrating cells, one set of our most important findings pertain to glioma cells in particular: even cells that are detached from the MTS can reorganize the matrix significantly, and these detached cells are quite prevalent in the stiffest matrices. We believe that understanding the patterns GBM forms down to the single-cell level is of importance for neurooncology research, especially for the development of antiinvasive strategies. More generally, unraveling details of how cancerous cells interact with ECM in its dual role as a physical barrier and a necessary tethering point for traction-based motion is of interest in cell biology. We believe the findings presented in this study represent a step forward in unraveling these details, and we further believe that the techniques used in this study, the implementation of simultaneous CARS and confocal reflectance microscopy, along with the comparison of microscopy with bulk rheology, have a bright future in cell biology.

## SUPPLEMENTARY MATERIAL

An online supplement to this article can be found by visiting BJ Online at <http://www.biophysj.org>.

The authors thank Peter Friedl, Fred Lanni, Jan Skotheim, and Andy Stein for valuable discussions. The authors also acknowledge the reviewers of this article, whose suggestions improved this article markedly.

This work was supported by a grant from the National Science Foundation through the Materials Research Science and Engineering Center (DMR-0213805) and by grants from the National Institutes of Health (CA 085139 and CA 113004). T.D. also acknowledges the support of the Harvard-MIT (HST) Athinoula A. Martinos Center for Biomedical Imaging and the Department of Radiology at Massachusetts General Hospital.

## REFERENCES

- Central Brain Tumor Registry of the United States (CBTRUS). 2002–2003. Primary Brain Tumors in the United States Statistical Report 1995–1999. CBTRUS, Chicago, IL.
- Tamariz, E., and F. Grinnell. 2002. Modulation of fibroblast morphology and adhesion during collagen matrix remodeling. *Mol. Biol. Cell.* 13:3915–3929.
- Cukierman, E., R. Pankov, D. R. Stevens, and K. M. Yamada. 2001. Taking cell-matrix adhesions to the third dimension. *Science.* 294:1708–1712.
- Brown, R. A., R. Prajapati, D. A. McGrouther, I. V. Yannas, and M. Eastwood. 1998. Tensional homeostasis in dermal fibroblasts: Mechanical responses to mechanical loading in three-dimensional substrates. *J. Cell. Physiol.* 175:323–332.
- Petroll, W. M., and L. Ma. 2003. Direct, dynamic assessment of cell-matrix interactions inside fibrillar collagen lattices. *Cell Motil. Cytoskeleton.* 55:254–264.
- Knapp, D. M., T. T. Tower, R. T. Tranquillo, and V. H. Barocas. 1999. Estimation of cell traction and migration in an isometric cell traction assay. *Am. Inst. Chem. Eng. J.* 45:2628–2640.
- Loftis, M. J., D. Sexton, and W. Carver. 2003. Effects of collagen density on cardiac fibroblast behavior and gene expression. *J. Cell. Physiol.* 196:504–511.
- Kuntz, R. M., and W. M. Saltzman. 1997. Neutrophil motility in extracellular matrix gels: Mesh size and adhesion affect speed of migration. *Biophys. J.* 72:1472–1480.
- Wolf, K., R. Muller, S. Borgmann, E. Brocker, and P. Friedl. 2003. Amoeboid shape change and contact guidance: T-lymphocyte crawling through fibrillar collagen is independent of matrix remodeling by MMPs and other proteases. *Blood.* 102:3262–3269.
- Friedl, P., K. Maaswer, C. E. Klein, B. Niggemann, G. Krohne, and K. S. Zanker. 1997. Migration of highly aggressive mv3 melanoma cells in 3-dimensional collagen lattices results in local matrix reorganization and shedding of  $\alpha 2$  and  $\beta 1$  integrins and cd44. *Cancer Res.* 57:2061–2070.
- Wolf, K., I. Mazo, H. Leung, K. Engelke, U. H. von Andrian, E. I. Deryugina, A. Y. Strongin, E. B. Brocker, and P. Friedl. 2003. Compensation mechanism in tumor cell migration: Mesenchymal-amoeboid transition after blocking of pericellular proteolysis. *J. Cell Biol.* 160:267–277.
- Maaser, K., K. Wolf, C. E. Klein, B. Niggemann, K. S. Zanker, E. Brocker, and P. Friedl. 1999. Functional hierarchy of simultaneously expressed adhesion receptors: Integrin  $\alpha 2 \beta 1$  but not cd44 mediates mv3 melanoma cell migration and matrix reorganization within three-dimensional hyaluronan containing collagen matrices. *Mol. Biol. Cell.* 10:3067–3078.
- Goldberg, W. J., K. V. Levine, G. Tadvalkar, E. R. Laws, Jr., and J. J. Bernstein. 1992. Mechanisms of c6 glioma cell and fetal astrocyte migration into hydrated collagen I gels. *Brain Res.* 581:81–90.
- Del Maestro, R., R. Shivers, W. McDonald, and A. Del Maestro. 2001. Dynamics of c6 astrocytoma invasion into three-dimensional collagen gels. *J. Neuro-Oncol.* 53:87–98.
- Cukierman, E., R. Pankov, and K. M. Yamada. 2002. Cell interactions with three-dimensional matrices. *Curr. Opin. Cell Biol.* 14:633–640.
- Gaudet, C., W. A. Marganski, S. Kim, C. T. Brown, V. Gunderia, M. Dembo, and J. Y. Wong. 2003. Influence of type 1 collagen surface density on fibroblast spreading, motility, and contractility. *Biophys. J.* 85:3329–3335.
- Ingber, D. E., and J. Folkman. 1989. Mechanochemical switching between growth and differentiation during fibroblast growth factor-stimulated angiogenesis in vitro: role of extracellular matrix. *J. Cell Biol.* 109:317–330.
- Lo, C.-M., H.-B. Wang, M. Dembo, and Y. Wang. 2000. Cell movement is guided by the rigidity of the substrate. *Biophys. J.* 79:144–152.
- Vernon, R. B., and E. H. Sage. 1996. Contraction of fibrillar type I collagen by endothelial cells: a study in vitro. *J. Cell. Biochem.* 60:185–197.
- Engler, A., L. Bacakova, C. Newman, A. Hategan, M. Griffin, and D. Discher. 2004. Substrate compliance versus ligand density in cell on gel response. *Biophys. J.* 86:617–628.
- Pelham, R. J., and Y. Wang. 1997. Cell locomotion and focal adhesions are regulated by substrate flexibility. *Proc. Natl. Acad. Sci. U S A.* 94:13661–13665.
- Gordon, V. D., M. T. Valentine, M. L. Gardel, D. Andor-Ardo, S. Dennison, A. A. Bogdanov, D. A. Weitz, and T. S. Deisboeck. 2003. Measuring the mechanical stress induced by an expanding multicellular tumor system: a case study. *Exp. Cell Res.* 289:58–66.
- Roy, P., W. M. Petroll, H. D. Cavanagh, C. J. Chuong, and J. V. Jester. 1997. An in vitro force measurement assay to study the early mechanical interaction between corneal fibroblasts and collagen matrix. *Exp. Cell Res.* 232:106–117.
- Galbraith, C. G., and M. P. Sheetz. 1997. A micromachined device provides a new bend on fibroblast traction forces. *Proc. Natl. Acad. Sci. U S A.* 94:9114–9118.
- Tan, J. L., J. Tien, D. M. Pirone, D. S. Gray, K. Bhadriraju, and C. S. Chen. 2003. Cells lying on a bed of microneedles: an approach to isolate mechanical force. *Proc. Natl. Acad. Sci. U S A.* 100:1484–1489.

26. Balaban, N. Q., U. S. Schwarz, D. Riveline, P. Goichberg, G. Tzur, I. Sabanay, D. Mahalu, S. Safran, A. Bershadsky, L. Addadi, and B. Geiger. 2001. Force and focal adhesion assembly: a close relationship studied using elastic micropatterned substrates. *Nat. Cell Biol.* 3: 466–472.
27. Shwarz, U. S., N. Q. Balaban, D. Riveline, A. Bershadsky, B. Geiger, and S. A. Safran. 2002. Calculation of forces at focal adhesions from elastic substrate data: The effect of localized force and the need for regularization. *Biophys. J.* 83:1380–1394.
28. Dembo, M., T. Oliver, A. Ishihara, and K. Jacobson. 1996. Imaging the traction stresses exerted by locomoting cells with the elastic substratum method. *Biophys. J.* 70:2008–2022.
29. Beningo, K. A., M. Dembo, I. Kaverina, J. V. Small, and Y. Wang. 2001. Nascent focal adhesions are responsible for the generation of strong propulsive forces in migrating fibroblasts. *J. Cell Biol.* 153:881–887.
30. du Roure, O., A. Saez, A. Buguin, R. H. Austin, P. Chavrier, P. Siberzan, and B. Ladoux. 2005. Force mapping in epithelial cell migration. *Proc. Natl. Acad. Sci. U S A.* 102:2390–2395.
31. Riveline, D., E. Zamir, N. Q. Balaban, U. S. Schwarz, T. Ishizaki, S. Narumiya, Z. Kam, B. Geiger, and A. D. Bershadsky. 2001. Focal contacts as mechanosensors: Externally applied local mechanical force induces growth of focal contacts by an mDia1-dependent and ROCK-independent mechanism. *J. Cell Biol.* 153:1175–1185.
32. Meshel, A. S., D. P. Nackashi, P. D. Franzon, and M. P. Sheetz. 2002. Single force measurements on 3D collagen matrix. *Biophys. J.* 82:411a. (Abstr.)
33. Freyman, T. M., I. V. Yannas, R. Yokoo, and L. J. Gibson. 2002. Fibroblast contractile force is independent of the stiffness which resists the contraction. *Exp. Cell Res.* 272:153–162.
34. Eastwood, M., R. Porter, U. Khan, G. McGrouther, and R. Brown. 1995. Quantitative analysis of collagen gel contractile forces generated by dermal fibroblasts and the relationship to cell morphology. *J. Cell. Physiol.* 166:33–42.
35. Friedl, P., and E.-B. Brocker. 2000. The biology of cell locomotion within three-dimensional extracellular matrix. *Cell. Mol. Life Sci.* 57: 41–64.
36. Meshel, A. S., Q. Wei, R. S. Adelstein, and M. P. Sheetz. 2005. Basic mechanism of three-dimensional collagen fibre transport by fibroblasts. *Nat. Cell Biol.* 7:157–164.
37. Velegol, D., and F. Lanni. 2001. Cell traction forces on soft biomaterials. 1. Microreology of type I collagen gels. *Biophys. J.* 81: 1786–1792.
38. Friedl, P., K. S. Zanker, and E. Brocker. 1998. Cell migration strategies in 3-D extracellular matrix: differences in morphology, cell matrix interactions, and integrin function. *Microsc. Res. Tech.* 43: 369–378.
39. Nan, X., J.-X. Cheng, and X. S. Xie. 2003. Vibrational imaging of lipid droplets with coherent anti-Stokes Raman scattering microscopy. *J. Lipid Res.* 44:2202–2208.
40. Nishikawa, R., X. D. Ji, R. C. Harmon, C. S. Lazar, G. N. Gill, W. K. Cavenee, and H. J. Huang. 1994. A mutant epidermal growth factor receptor common in human glioma confers enhanced tumorigenicity. *Proc. Natl. Acad. Sci. USA.* 91:7727–7731.
41. Sutherland, R. M. 1988. Cell and environment interactions in tumor microregions: The multicell spheroid model. *Science.* 240:177–184.
42. Kelm, J. M., N. E. Timmins, C. J. Brown, M. Fussenegger, and L. K. Nielsen. 2003. Method for generation of homogeneous multicellular tumor spheroids applicable to a wide variety of cell types. *Biotechnol. Bioeng.* 83:173–180.
43. Brightman, A. O., B. P. Rajwa, J. E. Sturgis, M. E. McCallister, J. P. Robinson, and S. L. Voytik-Harvin. 2000. Time-lapse confocal reflection microscopy of collagen fibrillogenesis and extracellular matrix assembly in vitro. *Biopolymers.* 54:222–234.
44. Saidi, I. S., S. L. Jaques, and F. K. Tittel. 1995. Mie and Rayleigh modeling of visible-light scattering in neonatal skin. *Appl. Opt.* 34: 7410–7418.
45. Duncan, M. D., J. Reintjes, and T. Manuccia. 1982. Scanning coherent anti-Stokes Raman microscope. *Opt. Lett.* 7:350–352.
46. Zumbusch, A., G. R. Holtom, and X. S. Xie. 1999. Three-dimensional vibrational imaging by coherent anti-Stokes Raman scattering. *Phys. Rev. Lett.* 82:4142–4145.
47. Cheng, J.-X., Y. K. Jia, G. Zheng, and X. S. Xie. 2002. Laser-scanning coherent anti-Stokes Raman scattering microscopy and applications to cell biology. *Biophys. J.* 83:502–509.
48. Cheng, J.-X., A. Volkmer, and X. S. Xie. 2002. Theoretical and experimental characterization of coherent anti-Stokes Raman scattering microscopy. *J. Opt. Soc. Am. B.* 19:1363–1375.
49. Cheng, J.-X., and X. S. Xie. 2004. Coherent anti-Stokes Raman scattering microscopy: instrumentation, theory, and applications. *J. Phys. Chem. B.* 108:827–840.
50. Potma, E. O., D. J. Jones, J.-X. Cheng, X. S. Xie, and J. Ye. 2002. High sensitivity coherent anti-Stokes Raman scattering microscopy with two tightly synchronized picosecond lasers. *Opt. Lett.* 27:1168–1170.
51. Williams, B. R., R. A. Gelman, D. C. Poppke, and K. A. Piez. 1978. Collagen fibril formation. *J. Biol. Chem.* 253:6578–6585.
52. Helmlinger, G., P. A. Netti, H. C. Lichtenbeld, R. J. Melder, and R. K. Jain. 1997. Solid stress inhibits the growth of multicellular tumor spheroids. *Nat. Biotechnol.* 15:778–783.
53. Darvish, K. K., and J. R. Crandall. 2001. Nonlinear viscoelastic effects in oscillatory shear deformation of brain tissue. *Med. Eng. Phys.* 23: 633–645.
54. Rossmurphy, S. B. 1992. Structure and rheology of gelatin gels—recent progress. *Polymer.* 33:2622–2627.
55. Miller, K., K. Chinzei, G. Orsengo, and P. Bednarz. 2000. Mechanical properties of brain tissue in-vivo: Experiment and computer simulation. *J. Biomech.* 33:1369–1376.
56. Schmidt, C. F., M. Barmann, G. Isenberg, and E. Sackmann. 1989. Chain dynamics, mesh size, and diffusive transport in networks of polymerized actin. A quasielastic light scattering and microfluorescence study. *Macromolecules.* 22:3638–3649.
57. Gibson, L. J., and M. F. Ashby. 1988. *Need Cellular Solids: Structure and Properties.* Pergamon, New York.
58. Ma, H.-S., A. P. Roberts, J.-H. Prevost, R. Jullien, and G. W. Scherer. 2000. Mechanical structure-property relationship of aerogels. *J. Non-Cryst. Solids.* 277:127–141.
59. MacKintosh, F. C., J. Kas, and P. A. Janmey. 1995. Elasticity of semiflexible biopolymer networks. *Phys. Rev. Lett.* 75:4425–4428.
60. Deisboeck, T. S., M. E. Berens, A. R. Kansal, S. Torquato, A. O. Stemmer-Reachamimov, and E. A. Chiocca. 2001. Pattern of self-organization in tumour systems: Complex growth dynamics in a novel brain tumour spheroid model. *Cell Prolif.* 34:115–134.
61. Nakano, A., E. Tani, K. Miyazaki, Y. Yamamoto, and J. Furuyama. 1995. Matrix metalloproteinases and tissue inhibitors of metalloproteinases in human gliomas. *J. Neurosurg.* 83:298–307.
62. Choe, G. Y., J. K. Park, L. Jouben-Steele, T. J. Kremen, L. M. Liau, H. V. Vinters, T. F. Cloughesy, and P. S. Mischel. 2002. Active mmp-9 expression is associated with primary glioblastoma subtype. *Clin. Cancer Res.* 8:2894–2901.
63. Nakada, M., H. Nakamura, E. Ikeda, N. Fujimoto, J. Yamashita, H. Sato, M. Seiki, and Y. Okada. 1999. Expression and tissue localization of membrane-type 1, 2, and 3 matrix metalloproteinases in human astrocytotic tumors. *Am. J. Pathol.* 154:417–428.
64. Wang, H., H. M. Wang, W. P. Shen, H. Huang, L. M. Hu, L. Ramdas, Y. H. Zhou, W. S. L. Liao, G. N. Fuller, and W. Zhang. 2003. Insulin-like growth factor binding protein 2 enhances glioblastoma invasion by activating invasion-enhancing genes. *Cancer Res.* 63:4315–4321.
65. Nabeshima, K., T. Inoue, Y. Shima, and T. Sameshima. 2002. Matrix metalloproteinases in tumor invasion: role for cell migration. *Pathol. Int.* 52:255–264.

66. Mackay, A. R., M. Ballin, M. D. Pelina, A. R. Farina, A. M. Nason, J. L. Hartzler, and U. P. Thorgeirsson. 1992. Effect of phorbol ester and cytokines on mmps and tissue inhibitor of metalloproteinase expression in tumor and normal cell lines. *Invasion Metastasis*. 12: 168–184.
67. Guido, S., and R. T. Tranquillo. 1993. A methodology for the systematic and quantitative study of cell contact guidance in oriented collagen gels: Correlation of fibroblast orientation and gel birefringence. *J. Cell Sci*. 105:317–331.
68. Beningo, K. A., and Y.-L. Wang. 2002. Flexible substrata for the detection of cellular traction forces. *Trends Cell Biol*. 12:79–84.
69. Chicoine, M. R., and D. L. Silbergeld. 1995. Assessment of brain tumor cell motility in vivo and in vitro. *J. Neurosurg*. 82:615–622.
70. Paulus, W., C. Huettner, and J. C. Tonn. 1994. Collagens, integrins and the mesenchymal drift in glioblastomas: A comparison of biopsy specimens, spheroid and early monolayer cultures. *Int. J. Cancer*. 58: 841–846.